Solar Energy 183 (2019) 392–397

Contents lists available at ScienceDirect

Solar Energy

journal homepage: www.elsevier.com/locate/solener

# The potential of scalability in high efficiency hybrid perovskite thin film luminescent solar concentrators

Benaz Mendewala[a], Katerina Nikolaidou[a], Christine Hoffman[b], Som Sarang[a], Jennifer Lu[c], Boaz Ilan[b], Sayantani Ghosh[a,*]

[a] Department of Physics, School of Natural Sciences, University of California, Merced, CA 95344, USA
[b] Department of Applied Mathematics, School of Natural Sciences, University of California, Merced, CA 95344, USA
[c] Department of Materials Science and Engineering, School of Engineering, University of California, Merced, CA 95344, USA

ARTICLE INFO

*Keywords:*
Hybrid perovskite
Luminescent solar concentrator
Thin film
Self-absorption
Optical efficiency

ABSTRACT

Hybrid metal-halide perovskite (PVSK) thin films have recently demonstrated exciting potential as candidates for broadband luminescent solar concentrators (LSCs). Here, we examine the correlation between film thickness, lead halide sources in the precursors, and film morphology, with the optical efficiency of planar PVSK LSCs with a view to optimizing device performance. After synthesizing and testing sixteen different types of PVSK samples, we report a maximum optical efficiency of 34.7% in $CH_3NH_3PbI_3$ LSC made with $Pb(Ac)_2$ precursor, and with optimal thickness in the 150–300 nm range. Using 3D Monte Carlo simulations that incorporate experimental results, we accurately estimate self-absorption and surface losses, and most importantly, demonstrate the possibility of scaling these LSCs up to almost 100 cm, thereby providing a route toward optimizing thin film PVSK materials for these and other optoelectronic and photovoltaic applications.

## 1. Introduction

Luminescent solar concentrators (LSCs) were originally introduced as a cost-effective alternative to traditional photovoltaic systems. Historically, LSCs have employed a polymer or glass substrates doped with fluorophores, such as quantum dots or dye molecules, to act as waveguides for down-converted sunlight to be directed to solar cells attached at their edges (Debije and Verbunt, 2012; Goetzberger and Greube, 1977; Shcherbatyuk et al., 2010; Weber and Lamb, 1976). LSC-based solar cells have many advantages when compared with traditional solar cells, and one of the most important of these is their ability to absorb both direct and diffuse sunlight. This allows LSCs to be incorporated into otherwise difficult architectures, such as vertical surfaces, and reduced cost for large area coverage (Kanellis et al., 2016; Sholin et al., 2007). Conventional optical concentration photovoltaic (CPV) technology uses concentrating optics to reduce solar cell area while maintaining high efficiency in order to commercially allow the use of higher efficiency and more costly solar cells relative to planar non-concentrated PV (Phillips et al., 2015). Typically, the CPVs employ Fresnel lenses or mirrors with single or dual axis tracking and have a typical concentration ration of 300–1000 for high concentration PV (HCPV). HCPV systems often utilize high efficiency, relatively expensive multi-junction solar cells such as GaInP/GaInS/Ge (Phillips et al., 2015). Efficiencies of commercially available CPV modules exceed 30%, with a Soitec model recently exhibiting 38.9% efficiencies at standard concentration (Dimroth et al., 2014).

Luminescent materials typically used in LSCs should ideally possess high quantum yield (QY), broadband absorption, and emission that is spectrally-matched to the band gap of the attached solar cell. Since the concept was introduced, LSC research has encompassed a wide array of materials. The most commonly used fluorescent components investigated include organic dyes and semiconductor quantum dots such as CdSe/CdS, CdSe/ZnS and PbS (Coropceanu and Bawendi, 2014; Hyldahl et al., 2009; Shcherbatyuk et al., 2010). The highest power conversion efficiency (PCE) to date is 7%, achieved in a dye-based LSC coupled to GaAs solar cells (Slooff et al., 2008). While this does not compare favorably with the performance of 1st and 2nd generation crystalline and thin film photovoltaics, it is close to the highest reported PCE of quantum dot-based solar cell (Liu et al., 2017). The biggest hurdle that prevents LSCs from practical implementation is not efficiency but scalability, which arises from 'self-absorption' (SA) losses. In most materials, the spectral overlap of the absorption and emission

*Abbreviations:* PVSK, perovskite; LSC, luminescent solar concentrator; PCE, power conversion efficiency; QY, quantum yield; SA, self-absorption; MAI, methylammonium iodide; ITO, indium tin oxide; PL, photoluminescence; SEM, scanning electron microscopy

* Corresponding author.
*E-mail address:* sghosh@ucmerced.edu (S. Ghosh).

https://doi.org/10.1016/j.solener.2019.03.042
Received 11 December 2018; Received in revised form 22 February 2019; Accepted 11 March 2019

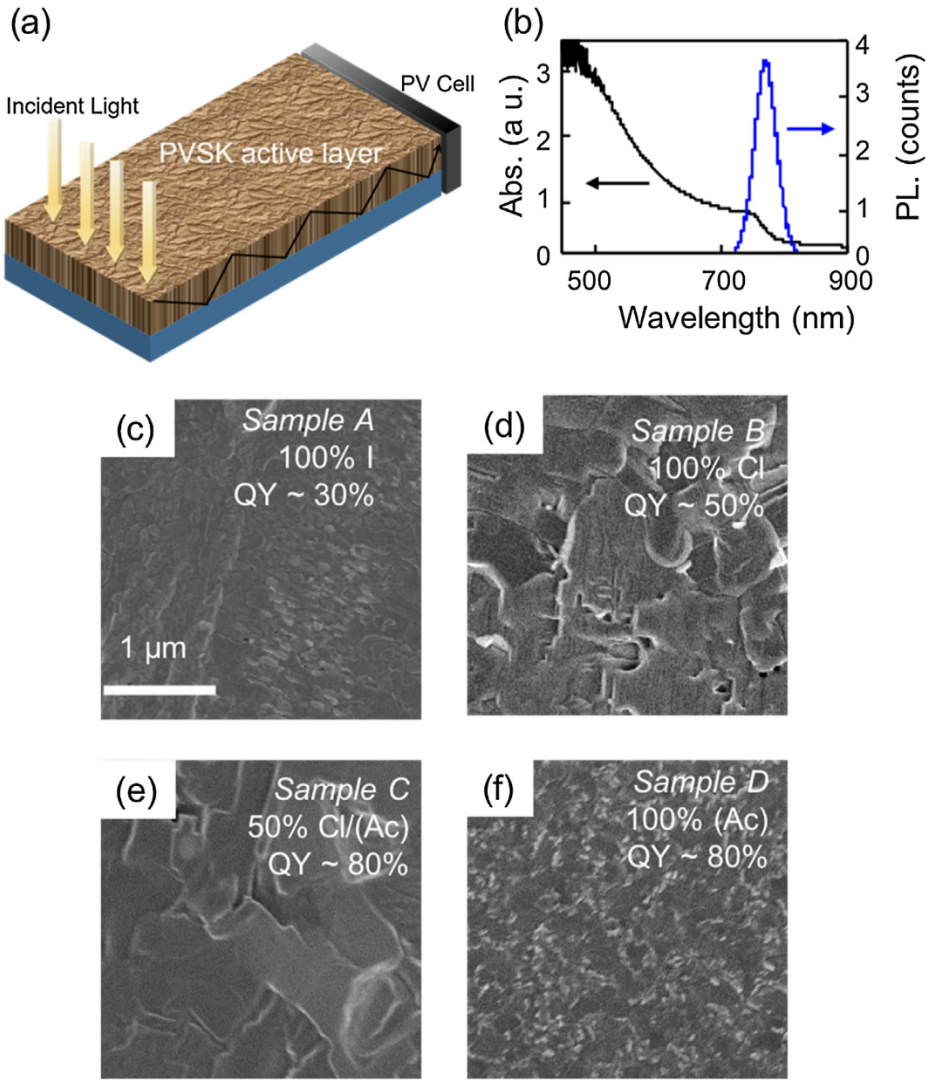


**Fig. 1.** Spectral and surface characterization. (a) Schematic of an LSC with a PV cell attached at one edge. (b) Absorption and PL spectra of a typical PVSK thin film. (c–f) Scanning electron microscope (SEM) images for samples A–D. All films are 450 nm thick.

bands results in the emitted light being re-absorbed by the material, and barring 100% QY, this results in further losses. There are two avenues to reducing SA: one is band gap engineering to induce a large spectral separation between absorption and emission bands, called Stokes shift (Meinardi et al., 2014); the other is to leverage materials with higher QY (Coropceanu and Bawendi, 2014). There has been some success with designing quantum dots with almost no SA losses, and although they have allowed the formation of relatively large LSCs, they have not necessarily translated to high efficiency devices (Brennan et al., 2018; Coropceanu and Bawendi, 2014; Zhao and Lunt, 2013). The best approach would therefore be to not focus on arresting SA alone, but to also invest in materials with high QY, which is the route we have taken.

Metal-halide hybrid perovskites (PVSKs) have been at the forefront of photovoltaic research for the past six years, owing to their rapidly improving PCE as thin film solar cells (Nie et al., 2015). The highest reported value currently stands at 22.7% (Green et al., 2018) compared to 22.9% for thin film calcogenide solar cells and 26.7% for Si crystalline solar cells. However, device stability remains a problematic issue, and success on that front has not kept up with advances in performance (Berhe et al., 2015). While recent perovskite solar cells have achieved stability under 1000 h of continuous illumination, this still falls far short of the 20-year lifetime expected for silicon solar cells (Christians et al., 2018). However, PVSKs are unique materials that have superior optical characteristics in conjunction with high carrier mobility and are highly suited for incorporation in LSCs as well as traditional solar cells (Even et al., 2014; Nikolaidou et al., 2016). Typical materials used for downconversion in LSCs include lanthanides and nanophosphors, but these are not as easily synthesized as PVSKs (de la Mora et al., 2017). While opaque thin films are generally not used in LSCs due to high self-absorption, in our prior work we observed that the high QY, broad absorption spectra, and large refractive index in hybrid PVSKs ($n = 2.5$) compensated exceedingly well for this shortcoming, achieving an impressive optical efficiency ($\eta_{opt}$) of 29% (Nikolaidou et al., 2016). Additionally, they remained stable over a period of months under ambient conditions (Nikolaidou et al., 2016). The flexibility of chemical composition of the hybrid PVSKs allows for many variations by using different halides (Cl, I, or Br) or even combinations of halides. Each of these composites have different quantum yields and absorption spectra, which create a very large phase space of parameters that will influence LSC performance. While optimal morphology for PVSK solar cells has been well researched (Salim et al., 2015), LSCs prioritize different qualities. In this work, we investigate the roles of halide composition, morphology and film thickness in PVSK based LSCs, and report an impressive experimental optical efficiency of 34.7%. In addition, 3D Monte Carlo simulations based on the data predict the PVSK properties could allow LSCs as large as 1 m.

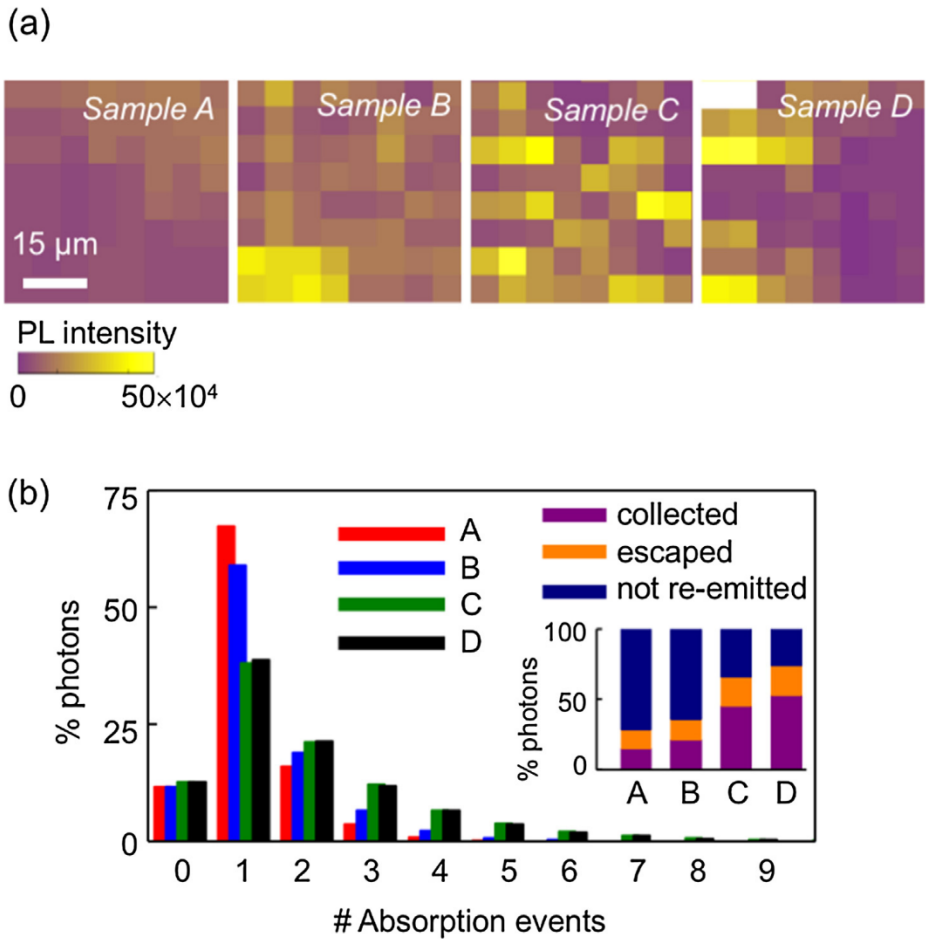


**Fig. 2.** Comparison of optical emission and absorption. (a) Spatially-resolved PL intensity scans of 40 $\mu m^2$ areas of the samples. (b) Histogram comparing simulated percentage of photons undergoing absorption events in the samples with film thickness 450 nm. (*inset*) Relative proportion of photons collected, lost, and re-emitted.

## 2. Experimental procedure

Our PVSK thin films are synthesized following established protocols (Nikolaidou et al., 2016). To systematically explore the phase space, we vary both film thickness and precursors, totaling sixteen different combinations. The solutions are prepared by adding purified (MAI) methylammonium iodide purchased from Luminescence Technology Corp. to N,N-Dimethylformamide (DMF) solvent, followed by the relevant lead halide compound, $PbCl_2$, $PbI_2$ or $Pb(Ac)_2$, all purchased from Sigma-Aldrich. The mixture is sonicated for one minute, and then stirred overnight in a $N_2$ glovebox. The films are prepared from this mixture by spin-coating on indium tin oxide (ITO) coated glass substrates at 3000–6000 rpm for 30 s to produce thicknesses ranging from 150 to 600 nm, followed by annealing on a hot plate at 100–120 °C for 30 min–2 h. The annealing time is dependent upon the by-product evaporation rate, which is much faster for samples containing acetate, while samples containing iodide and/or chloride are on the slower end, taking upwards of an hour to anneal the thickest samples. The samples remain in the glovebox throughout the spin-coating and annealing process and are removed and exposed to ambient conditions only when ready for measurements. The thickness of each sample is measured using cross-sectional SEM imaging using FESEM (Zeiss, ULTRA-55) with secondary electrons as the signal type. Top-down SEM images are then taken of all the samples to observe surface characteristics. These films also undergo typical characterization including x-ray diffraction (Nikolaidou et al., 2016; Ishihara et al., 2016).

Fig. 1(a) is a schematic of our device architecture. The PVSK thin film forms the active material which absorbs normally incident sunlight and transmits the down-converted emission to standard silicon (Si) photovoltaic (PV) cells attached perpendicular to the surface along the edge. For optical efficiency measurements, we measured current from the Si cells in ambient sunlight with and without our LSCs and calculated optical efficiency using $\eta_{opt} = \frac{I_{LSC} \times A_{PV}}{I_{PV} \times A_{LSC}}$, where the geometric gain is defined as the ratio of the areas of the LSCs and PV cells attached at the edges and, considering the entire circumference, is 3.75 for our samples. Absolute QYs of thin films is a notoriously difficult measurement, especially given these are highly inhomogeneous polycrystalline samples. We therefore estimated QY using an Acton SP2300 spectrophotometer relative to a standard laser dye. Self-absorption (SA) is measured by collecting emission from the sample edge after exciting our thin films with a broadband white light source. By varying the pump-detector distance and measuring the resulting intensity drop in emission, we quantified the SA loss. We also performed spatially resolved photoluminescence (PL) scans at normal incidence using a continuous wave laser source tuned to 408 nm.

## 3. Results

Fig. 1(b) is a representative plot highlighting the broad absorption band and near infrared emission spectrum of one of the PVSK samples. Fig. 1(c)–(f) are scanning electron microscopy (SEM) images of a subset of our samples that highlight the differences caused by the different halide precursors during synthesis. The halide precursors (final compositions) for samples A–D are $PbI_2$ ($CH_3NH_3PbI_3$), $PbCl_2$ ($CH_3NH_3PbI_{3-x}Cl_x$), 1:1 mixture of $PbCl_2$ and $Pb(Ac)_2$ ($CH_3NH_3PbI_{3-x}Cl_x$), and $Pb(Ac)_2$ ($CH_3NH_3PbI_3$), respectively. Samples A and D are both pure halide

PVSKs and have the same final composition, but as the SEM images show, the morphology is very different. The same is true for samples B and C, which are both mixed halide PVSKs. The use of different precursors influences the surface greatly, since each precursor produces different by-products that evaporate at varied rates (Salim et al., 2015; Sharenko and Toney, 2016). Faster evaporation rates lead to smaller grains and smoother surfaces (Salim et al., 2015; Sharenko and Toney, 2016; Zhang et al., 2015). Consequently, $PbCl_2$ tends to produce larger crystalline grains while $Pb(Ac)_2$ leads to smaller crystals but a smoother morphology, and these trends are supported by our SEM images. The effect of sample crystallinity on emission properties is a complex and slightly debated topic. Theoretical models show PVSK grain boundaries to be intrinsically benign relative to other polycrystalline materials (Yin et al., 2014), but experimental studies contend that they might act as trap sites, increasing non-radiative recombination (de Quilettes et al., 2015). The relative QY for A–D averaged over several samples of each type is noted in the figure as well, and indicate that the presence of $Pb(Ac)_2$ improves the yield.

Fig. 2 is a comparison of optical emission and absorption of the four samples. Fig. 2(a) is a set of spatially resolved scanning PL maps where the optical emission is collected at normal incidence. Integrating the emission over the scanned spatial area indicates sample A has the lowest PL count, sample B being next while samples C and D on average have the highest. This variation highlights the critical role of precursors in PVSK morphology and how that affects optical yield and characteristics. $PbCl_2$ in the precursors enhances crystallinity due to slow by-product evaporation rate (Salim et al., 2015), which should reduce non-radiative recombination, while the presence of $Pb(Ac)_2$ is known to suppress the growth of large crystals, increasing the grain density and the sites of non-radiative losses through the proliferation of grain boundaries (Zhang et al., 2015). We incorporate the absorption and emission data from Figs. 1 and 2 into 3D Monte Carlo simulations that use the model of a box-shaped LSC, with dimensions of 5 cm × 5 cm × thickness $t$, whose top surface points toward the sun, the bottom is attached to a perfect mirror, and the side edges are covered by solar cells. The normally incident radiation is sampled from the terrestrial solar spectrum (Debije et al., 2009) and assumed to be Lambertian. Propagation distances inside the material are based on inverting the Beer-Lambert law (Şahin et al., 2013) using measured absorbance and emission spectra. Photons absorbed by the material are probabilistically emitted isotropically based on the chance on non-radiative recombination and the material emission spectra. Photons striking the top surface are probabilistically reflected or transmitted based on Fresnel reflectance with a measured substrate refractive index of $n = 1.7$ to account for the ITO coating (the results are similar using $n = 1.5$). Snell reflection is employed on the bottom surface and on reflected photons at the top surface. Photons are monitored until they strike a side edge where they would be collected by a solar cell, escape back through the top surface, or are lost by non-radiative routes and therefore not re-emitted. We also monitor the number of times each photon is absorbed. In Fig. 2(b) the main bar plot charts the percentage of photons undergoing a specific number of absorption events in the four samples. '0' represents incidents photons that are not absorbed at all, which account for 12–15% of the incident excitation. This proportion is consistent for all PVSKs irrespective of composition given the film thicknesses are the same. Beyond that, sample A has the highest absorbance, as noted by the largest proportion of '1' (first) absorption event. It also has the lowest probability for more absorption events ('#' > 1) which ought to translate to low self-absorption (SA) losses. The inset compiles the proportions of photons that escape, are not re-emitted, and are collected by solar cells at the edges. There is a clear monotonic increase in the percentage of collected photons from samples A-D that follows the QY trend of Fig. 1(c)–(f) and suggests that high QY is indeed capable of overcoming SA losses. Additional detalk about the simulations are available in the supplementary document.

We obtain a quantifiable measure of SA losses in the LSCs in Fig. 3.

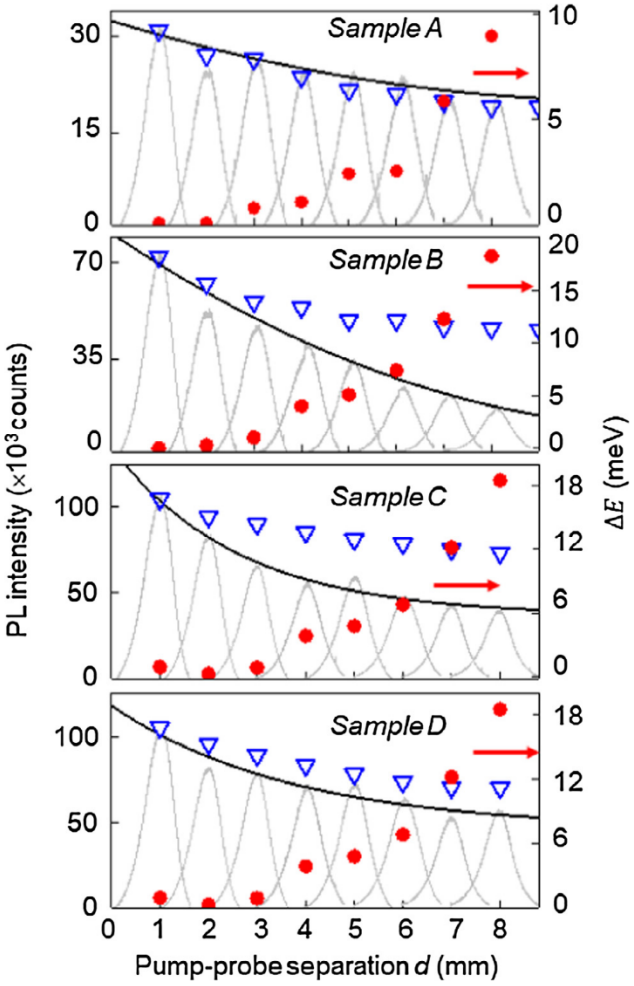


**Fig. 3.** Estimating self-absorption. PL spectra (gray curves) at increasing pump-probe separation shown to demonstrate emission intensity loss along the length of the LSCs designed from samples A–D. Peak intensity as function of the same separation is superposed in black on the spectral curves. Simulated percentage of photons collected (downward triangles) and emission peak energy shift (filled circles) with varying $d$ are also shown for every sample.

The samples are excited normally with a white light source focused down to a 1 μm spot and PL is collected from the edge as the separation between excitation and collection $d$ is varied by laterally translating the excitation spot. The PL curves (gray) of samples A–D show a steady drop in emission intensity with increasing $d$, as is expected given the QY is always less than 100%. In addition to intensity reduction, the process of re-absorption and re-emission results in an overall red-shift of the PL spectra (Nikolaidou et al., 2016). We track the peak emission wavelength with $d$ and plot the difference between it and the $d = 0$ value as $\Delta E$ (circles) for each sample. At first glance it appears as though sample A has the best outcome, where the intensity reduces by less than 40% and the spectral shift is ~8 meV; but the initial low PL due to the small QY puts it at a disadvantage. Sample B has the worst SA losses, and despite having a higher QY, sample C does not seem to translate that to superior SA properties. Sample D possesses the best combination of high QY and acceptable SA losses with the emission falling to 43% as the light traverses the sample length. This is still a substantial loss compared to other active materials (Yin et al., 2014), but not unexpected, considering the active medium is a continuous film, not comprised of discrete dopants. Further, the trend in the edge emission data of sample D indicates the intensity drop is leveling off, which is a positive attribute that could allow for scaling up of device dimensions.

We investigate the scalability aspect next through simulations.

Based on the same LSC model used to generate the data in Fig. 2(b), we calculate SA losses in the LSCs. In this exercise, the distance that a photon travels until it is absorbed is determined using Beer-Lambert's law, based on the (corrected) absorption spectrum (see Berhe et al., 2015 for details). Once absorbed, the probability of this photon to be re-emitted is the QY. If re-emitted, the red-shifted wavelength and the emitted intensity is sampled from the emission spectrum and the photon's direction is chosen randomly assuming isotropic emission. The calculated spectrally-integrated emission intensities as functions of $d$ are plotted in Fig. 3 for samples A–D (triangles) normalized to the experimental results. There is good agreement between simulation and data for samples A and D, both of which are pure iodide films. The same is not the case for the mixed halide $CH_3NH_3PbI_{3-x}Cl_x$ samples, B and C. Revisiting Fig. 2(a), we can see that the PL maps of samples B and C have more of a checkerboard pattern, becoming spatially non-uniform because of the larger grains that are typical when $PbCl_2$ is used as a precursor. This inhomogeneity is not incorporated in this simple fitting model. However, as this model seems to work well in samples A and D with smaller grains, we extend the scope of the MC simulations to larger sample sizes. Once again, the calculations use the measured absorption and emission data. However, there is significant SA in all the samples, which, for $\lambda > 760$ nm, is "in the noise" of the absorption data. To address this issue, we take one measured PL value, corresponding to $d = 1$ mm, and use it to fit the tail of the absorption spectrum as exponentially decreasing beyond 760 nm. We then use this "corrected" absorption spectrum to generate the computational results for larger LSCs and plot the calculated percentage of photons at varying $d$ in Fig. 4. Not surprisingly, samples A and B prove unsuited for use in realistic devices, with less than 5% of total incident light available for collection beyond 1 cm from the point of illumination. Samples C and D show more encouraging trends and the latter has 28% of the initial emission available for collection after traversing 100 cm. For comparison, the largest LSC so far, with a size ~100 cm has shown an optical efficiency of 4.5%. The other parameter that affects LSC performance is the film thickness. PVSKs are advantageous in that they absorb very efficiently over the entire visible spectrum, but highly absorptive thick films also ratchet up the SA. Solar cell design focuses on ultrathin films (< 150 nm) to maximize carrier extraction, but concentrators do not have this restraint. Experimental optical efficiency $\eta_{opt}$ values are summarized in Fig. 5. Surprisingly, experimental $\eta_{opt}$ is very similar for samples A–C that have disparate QYs. Sample D, where there is a small non-monotonicity, with the highest $\eta_{opt}$ of 34.7% observed at $t = 300$ nm followed by reduced efficiency with increasing thickness. Taken together, this leads us to the conclusion that thin films synthesized using 100% $Pb(Ac)_2$ precursors such as sample D behave most like homogenous active media. This is expected from the SEM images that confirm a smooth morphology. Samples A–C behave atypically, which we attribute to the morphological non-uniformity that lowers QY and negates any gain from enhanced absorption.

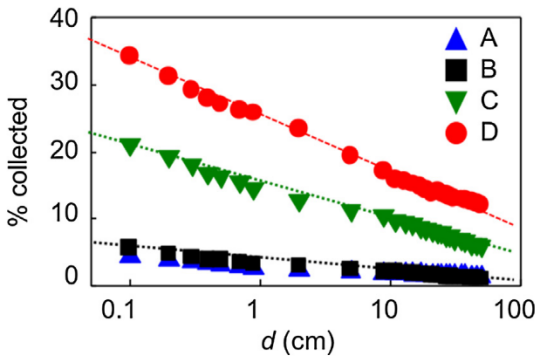


**Fig. 4.** Simulation of self-absorption in large scale LSCs plotted with excitation-collection separation.

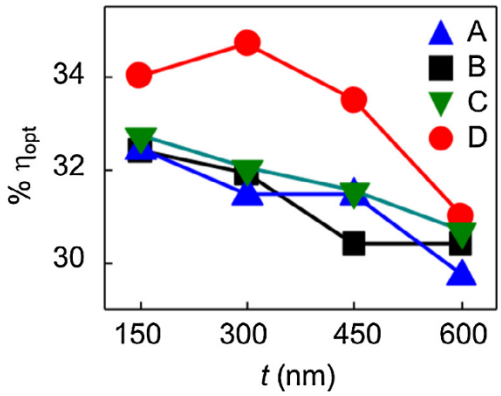


**Fig. 5.** Optical efficiency experimentally measured for LSCs as a function of film thickness in the various composites.

## 4. Conclusion

Perovskite thin films are shown to be excellent candidates for LSCs. By optimizing the morphology and thickness of the sample, we can achieve a maximum optical efficiency of 34.7%, with a minimum of 29.7%. This is a result of perovskite materials having overall high quantum yield, large Stokes shift, and large refractive index. The incorporation of acetate makes a smooth film that allows light to travel to the sample edges with minimal self-absorption, resulting in a high-efficiency LSC. While thicker samples increase absorption, the increased self-absorption is detrimental in all except the highest quantum yield samples, giving better results with thinner films. For most samples, film thickness of 150 nm achieved the best performance. Additionally, the emission wavelength is favorable for silicon photovoltaics, showing promise for incorporation into large scale photovoltaic systems. While our results reveal the critical role of $Pb(Ac)_2$ in sample synthesis, intriguingly, all samples show high $\eta_{opt}$, once again confirming the suitability of hybrid PVSKs as LSC material. MC simulations corroborate our results, suggesting that SA losses can be overcome by high QY and allow for scaling up of devices. While commercialization of perovskite LSCs will require improvements in device stability, toxicity and synthesis, existing technical options can address these to a large extent. For example, encapsulation of the device in glass would provide resistance from eroding due to moisture and oxygen, while also preventing exposure to a lead environment. Further improvements can be made to the device by engineering the substrate and the geometry for improved optical efficiency. Our investigations also highlight the issues that affect accurate evaluation of PVSK materials, chief among them being how QY is measured and incorporated into device modeling. As the discrepancy between the calculated and experimental results in Fig. 2 highlights, global QY estimation is an unreliable estimate of non-radiative recombination losses in a sample with a morphology as inhomogeneous as observed in these materials. Correlations between morphology and emission at high spatial resolution as we have shown here is an important step towards providing an accurate prediction, not only as concentrators, but also as solar cells.

## Acknowledgements

This research was supported by funds from the National Aeronautics and Space Administration (NASA) grant no. NNX15AQ01A.

## Appendix A. Supplementary material

Supplementary data to this article can be found online at https://doi.org/10.1016/j.solener.2019.03.042.

## References


Berhe, T.A., Su, W., Chen, C., Pan, C., Cheng, J., Chen, H., Tsai, M., Chen, L., Dubale, A.A., Hwang, B., 2015. Organometal halide perovskite solar cells: degradation and stability. Energy Environ. Sci. 9, 323–356.

Brennan, L.J., Purcell-Milton, F., McKenna, B., Watson, T.M., Gun'koab, Y.K., Evans, R.C., 2018. Large area quantum dot luminescent solar concentrators for use with dye-sensitised solar cells. J. Mater. Chem. A 6, 2671–2680.

Christians, J.A., Schulz, P., Tinkham, J.S., Schloemer, T.H., Harvey, S.P., Tremolet de Villers, B.J., Sellinger, A., Berry, J.J., Luther, J.M., 2018. Tailored interfaces of unencapsulated perovskite solar cells for > 1,000 hour operational stability. Nat. Energy 3, 68–74.

Coropceanu, I., Bawendi, M.G., 2014. Core/shell quantum dot based luminescent solar concentrators with reduced reabsorption and enhanced efficiency. Nano Lett. 14, 4097–4101.

de la Mora, M.B., Amelines-Sarria, O., Monroy, B.M., Hernández-Pérez, C.D., Lugo, J.E., 2017. Materials for downconversion in solar cells: perspectives and challenges. Sol. Energy Mater. Sol. Cells 165, 59–71.

de Quilettes, D.W., Vorpahl, S.M., Stranks, S.D., Nagaoka, H., Eperon, G.E., Ziffer, M.E., Snaith, H.J., Ginger, D.S., 2015. Impact of microstructure on local carrier lifetime in perovskite solar cells. Science 348, 683–686.

Debije, M.G., Teunissen, J., Kastelijn, M.J., Verbunt, P.P.C., Bastiaansen, C.W.M., 2009. The effect of a scattering layer on the edge output of a luminescent solar concentrator. Sol. Energ. Mat. Sol. Cells 93, 1345–1350.

Debije, M.G., Verbunt, P.P.C., 2012. Thirty years of luminescent solar concentrator research: solar energy for the built environment. Adv. Energy Mater. 2, 12–35.

Dimroth, F., Grave, M., Beutel, P., Fiedeler, U., Karcher, C., Tibbits, T.N.D., Oliva, E., Siefer, G., Schachtner, M., Wekkeli, A., Bett, A.W., Krause, R., Piccin, M., Blanc, N., Drazek, C., Guiot, E., Ghyselen, B., Salvetat, T., Tauzin, A., Signamarcheix, T., Dobrich, A., Hannappel, T., Schwarzburg, K., 2014. Wafer bonded four-junction GaInP/GaAs//GaInAsP/GaInAs concentrator solar cells with 44.7% efficiency. Prog. Photovolt. Res. Appl. 3, 277–282.

Even, J., Pedesseau, L., Katan, C., 2014. Analysis of multivalley and multibandgap absorption and enhancement of free carriers related to exciton screening in hybrid perovskites. J. Phys. Chem. C 118, 11566–11572.

Goetzberger, A., Greube, W., 1977. Solar energy conversion with fluorescent collectors. Appl. Phys. 14, 123–139.

Green, M.A., Hishikawa, Y., Warta, W., Dunlop, E.D., Levi, D.H., Hohl-Ebinger, J., Ho-Baillie, A.W.Y., 2018. Solar cell efficiency tables (Version 52). Prog. Photovolt. Res. Appl. 26, 427–436.

Hyldahl, M.G., Bailey, S.T., Wittmershaus, B.P., 2009. Photo-stability and performance of CdSe/ZnS quantum dots in luminescent solar concentrators. Sol. Energy 83, 566–573.

Ishihara, H., Chen, W., Yen-Chang, Chen, Sarang, S., Marco, N.D., Lin, O., Ghosh, S., Tung, V., 2016. Electrohydrodynamically assisted deposition of efficient perovskite photovoltaics. Adv. Mater. Interf. 3, 1500762. https://doi.org/10.1002/admi.201500762.

Kanellis, M., de Jong, M.M., Slooff, L., Debije, M.G., 2016. The solar noise barrier project: 1. Effect of incident light orientation on the performance of a large-scale luminescent solar concentrator noise barrier. Renew. Energy 103, 647–652.

Liu, M., Voznyy, O., Sabatini, R., García de Arquer, F.P., Munir, R., Balawi, A.H., Lan, X., Fan, F., Walters, G., Kirmani, A.R., Hoogland, S., Laquai, F., Amassian, A., Sargent, E.H., 2017. Hybrid organic–inorganic inks flatten the energy landscape in colloidal quantum dot solids. Nat. Mater. 16, 258–263.

Meinardi, F., Colombo, A., Velizhanin, K.A., Simonutti, R., Lorenzon, M., Beverina, L., Viswanatha, R., Klimov, V.I., Brovelli, S., 2014. Large-area luminescent solar concentrators based on 'Stokes-shift-engineered' nanocrystals in a mass-polymerized PMMA matrix. Nat. Photon. 8, 392–399.

Nie, W., Tsai, H., Asadpour, R., Blancon, J.C., Neukirch, A.J., Gupta, G., Crochet, J.J., Chhowalla, M., Tretiak, S., Alam, M.A., Wang, H.L., Mohite, A.D., 2015. High-efficiency solution-processed perovskite solar cells with millimeter-scale grains. Science 347, 522–525.

Nikolaidou, K., Sarang, S., Hoffman, C., Mendewala, B., Ishihara, H., Lu, J.Q., Ilan, B., Tung, V., Ghosh, S., 2016. Hybrid perovskite thin films as highly efficient luminescent solar concentrators. Adv. Opt. Mater. 4, 2126–2132.

Phillips, S.P., Bett, A.W., Horowitz, K., Kurtz, S., 2015. Current Status of Concentrator Photovoltaic (CPV) Technology. Web. https://doi.org/10.2172/1351597.

Şahin, D., Ilan, B., 2013. Radiative transport theory for light propagation in luminescent media. J. Opt. Soc. Am. A 30 (5), 813–820.

Salim, T., Sun, S., Abe, Y., Krishna, A., Grimsdale, A.C., Lam, Y.M., 2015. Perovskite-based solar cells: impact of morphology and device architecture on device performance. J. Mater. Chem. A 3, 8943–8969.

Sharenko, A., Toney, M.F., 2016. Relationships between lead halide perovskite thin-film fabrication, morphology, and performance in solar cells. J. Am. Chem. Soc. 138, 463–470.

Shcherbatyuk, G.V., Inman, R.H., Wang, C., Winston, R., Ghosh, S., 2010. Viability of using near infrared PbS quantum dots as active materials in luminescent solar concentrators. Appl. Phys. Lett. 96, 191901.

Sholin, V., Olson, J.D., Carter, S.A., 2007. Semiconducting polymers and quantum dots in luminescent solar concentrators for solar energy harvesting. J. Appl. Phys. 101, 123114.

Slooff, L.H., Bende, E.E., Burgers, A.R., Budel, T., Pravettoni, M., Kenny, R.P., Dunlop, E.D., Büchtemann, A., 2008. A luminescent solar concentrator with 7.1% power conversion efficiency. Phys. Status Solidi – Rapid Res. Lett. 2, 257–259.

Weber, W.H., Lambe, J., 1976. Luminescent greenhouse collector for solar radiation. Appl. Opt. 15, 2299.

Yin, W.J., Shi, T., Yan, Y., 2014. Unique properties of halide perovskites as possible origins of the superior solar cell performance. Adv. Mater. 26, 4653–4658.

Zhang, W., Saliba, M., Moore, D.T., Pathak, S.K., Hörantner, M.T., Stergiopoulos, T., Stranks, S.D., Eperon, G.E., Alexander-Webber, J.A., Abate, A., Sadhanala, A., Yao, S., Chen, Y., Friend, R.H., Estroff, L.A., Wiesner, U., Snaith, H.J., 2015. Ultrasmooth organic–inorganic perovskite thin-film formation and crystallization for efficient planar heterojunction solar cells. Nat. Commun. 6, 6142.

Zhao, Y., Lunt, R.R., 2013. Transparent luminescent solar concentrators for large-area solar windows enabled by massive stokes-shift nanocluster phosphors. Adv. Energy Mater. 3, 1143–1148.

Supplementary Information for the Monte Carlo Simulations

A sketch of the Monte Carlo algorithm is depicted in Figure 1 below.

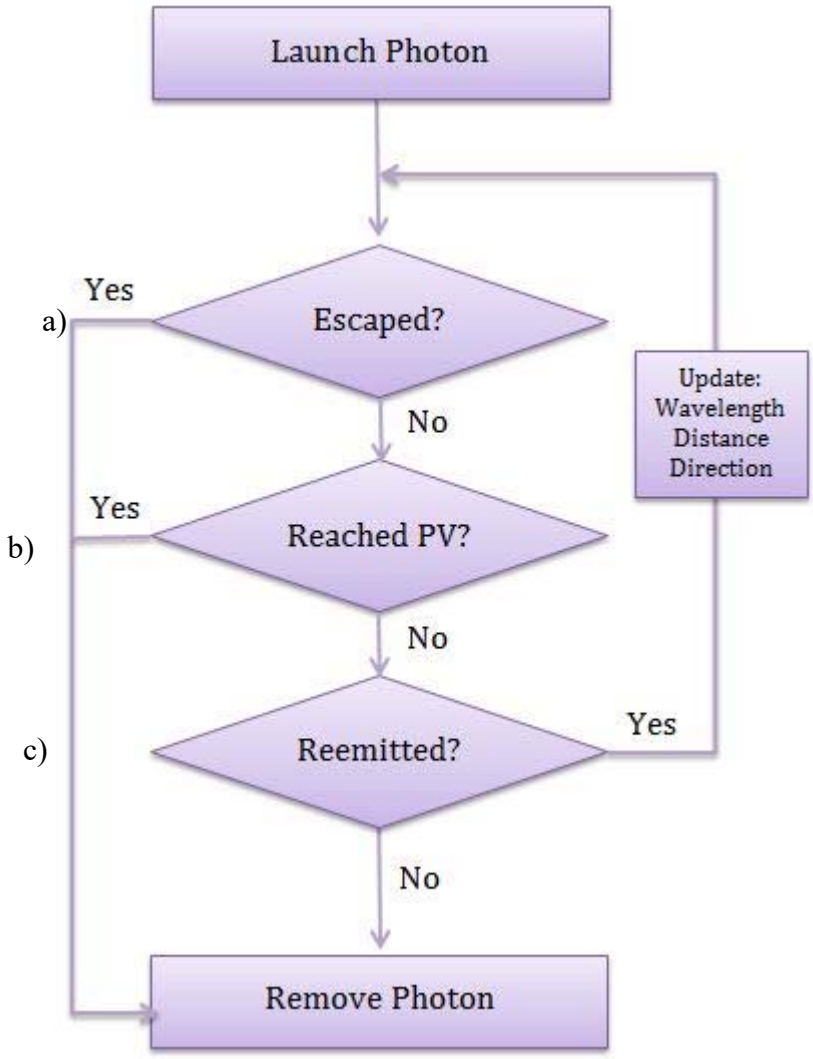


**Figure 1.** Sketch of the Monte Carlo algorithm. "Photons" are launched into the 3D LSC box from the top surface and the distance traveled until its next absorption is calculated. The route traveled by the photon over this distance is analyzed to confirm that the photon did not reach one of the LSC sides. The absorbed photon is reemitted probabilistically based on the QY in an isotropic direction (uniformly random angle cosines) with a wavelength sampled randomly from on the emission spectrum. The process repeats all the photons have either reached the PV cells where they are collected, escaped through the top surface, or lost due to non-radiative routes.

The LSC is modeled as a box (450 nm thick) with the solar radiation on the top surface. A total of $5 \cdot 10^5$ photons are launched. Solar radiation is sampled from the terrestrial solar spectrum (Emery et al., 2000) in the range of 280nm – 850 nm and assumed to be Lambertian around normal incidence.

Propagation distances inside the material are based on inverting the Beer-Lambert law (Şahin et al., 2013) using the measured absorbance and emission spectra (see for example Figure 2 below).

Above 760nm the measured absorbance falls within the noise level. Since the overall theoretical efficiency of the LSC is sensitive to this "cutoff wavelength", we vary the absorption spectrum as exponentially decaying from its value at 760nm with a decay exponent that is fitted to the measured PL data. Photons absorbed by the material are probabilistically reemitted based on the measured QY. If reemitted, the phtons are reemitted in an isotropic direction (uniformly random angle cosines) with a wavelength that is sampled randomly from on the measured emission spectrum.

Photons striking the top surface are randomly reflected or transmitted based on Fresnel transmission and reflection formulae for unpolarized light with a measured substrate refractive index of $n$ = 1.7 to account for the ITO coating (the results are similar using $n$ = 1.5). Snell reflection is employed on the bottom surface and at the top surface from within the box.

The photons are monitored until they strike a side edge where they are collected by a solar cell, escape the top surface, or lost by non-radiative routes. The number of times each photon is (re)absorbed is recorded for generating the data in Figure 2 in the main text.

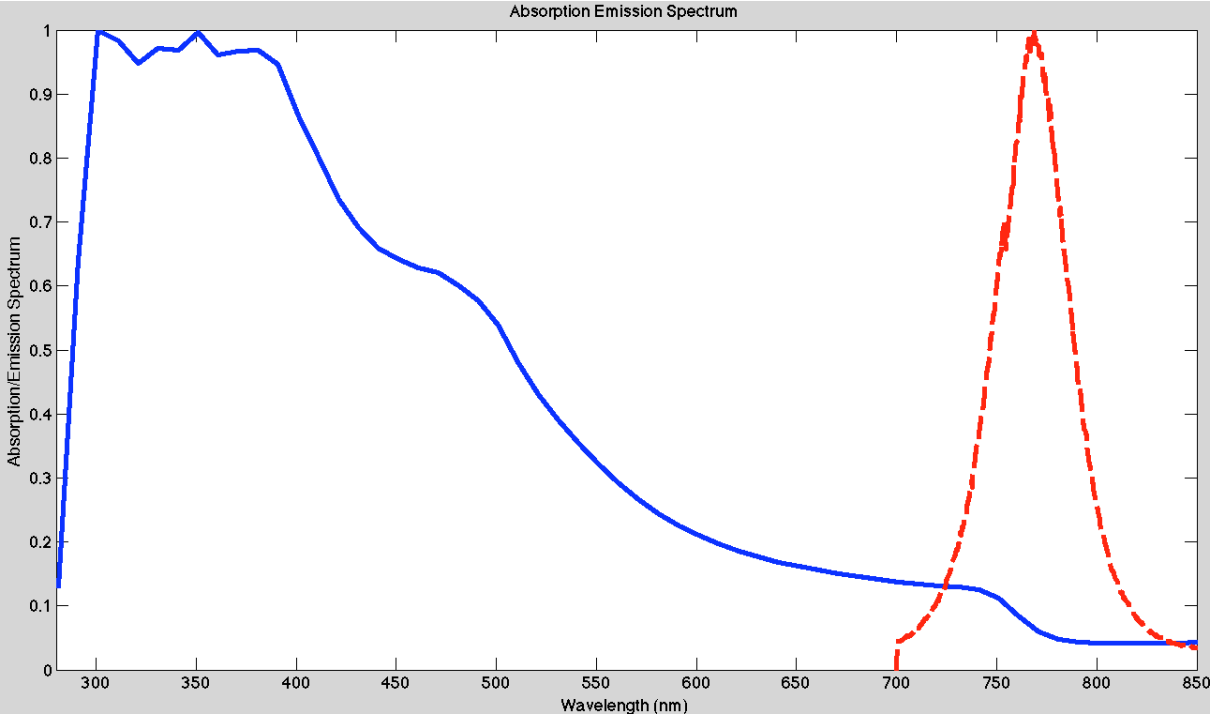


**Figure 2.** Normalized measured absorption (blue) and emission (red) spectra for one of the sample materials.

K. Emery, "Reference solar spectral irradiance: Air mass 1.5," 560 Tech. rep. (ASTM, 2000), http://rredc.nrel.gov/solar/spectra/ 561 am1.5.